



# Magnetron sputtering of titanium carbonitride nanocomposite coatings — Does the choice of carbon source affect film properties?

Juliana Kessler<sup>a</sup>,<sup>\*</sup> Olivier Donzel-Gargand<sup>b</sup>, Dmitrii Moldarev<sup>c</sup>, Claudia Franzén<sup>a</sup>, Daniel Primetzhofer<sup>c</sup>, Ulf Jansson<sup>a</sup>, Erik Lewin<sup>a</sup>

<sup>a</sup> Department of Chemistry – Ångström Laboratory, Uppsala University, Box 538, Uppsala, SE-751 21, Sweden

<sup>b</sup> Department of Materials Science and Engineering, Uppsala University, Box 35, Uppsala, SE-751 21, Sweden

<sup>c</sup> Department of Physics and Astronomy, Uppsala University, Box 516, Uppsala, SE-751 21, Sweden

## ARTICLE INFO

### Keywords:

Fuel cells  
Bipolar plates  
Carbonitride  
Magnetron sputtering  
Nanocomposite  
Ti–C–N

## ABSTRACT

We report on a study of titanium carbonitride coatings, with potential applications as protective coatings on bipolar plates in fuel cells. Two series of Ti–C–N coatings with a carbon concentration varying between 8 and 34 at.% were deposited by magnetron sputtering, using a graphite target or methane gas as carbon source. Characterisation with X-ray diffraction, ion beam analysis, Raman spectroscopy and electron microscopy shows that the coatings consist of a crystalline titanium carbonitride phase and an amorphous carbon tissue phase: nc-Ti(C,N)/a-C(:N). It was found that the mechanical and electrical properties are primarily dependent on the carbon content and not the choice of carbon source. An increase in C content leads to a decreasing crystallite size and an increasing amount of amorphous carbon. Thus, the phase content and microstructure and thereby the properties are controlled by the carbon content, making the nc-Ti(C,N)/a-C(:N) coatings highly tuneable. Depending on C content hardness of 11–38 GPa and resistivity of 150–623  $\mu\Omega\text{cm}$  was observed. Additionally, the coatings were found to exhibit a contact resistance against silver that was 10 times lower than that of a stainless steel reference. This makes titanium carbonitride nanocomposite coatings promising candidates for the use on bipolar plates in fuel cells.

## 1. Introduction

The transition to sustainable energy solutions is presently one of the greatest challenges that human society faces. Hence, the development of materials, and in particular coating materials, is a crucial part of the solution. One field where coatings will be essential is the field of electrochemical cells and in particular proton electrolyte membrane fuel cells (PEMFC), where hydrogen is used to generate electricity forming only water and heat as by-products. In PEMFCs, bipolar plates (BPP) are an integral part directing flows of gas to the reactive sites, acting as current collectors, heat conductors and ensuring the structural integrity of the fuel cell. Compared to graphite, stainless steel BPPs offer the advantage of inherent malleability, which enables the production of thinner plates cutting weight, volume and thereby reducing costs [1–3]. However, stainless steel BPPs lack corrosion resistance in the operating environment of a fuel cell. A simple and cost-efficient method to modify surface properties is by coating the BPPs, thereby increasing e.g. corrosion resistance. Recent studies have demonstrated that the potential at the surface of stainless steel BPPs is not as high as previously anticipated and that they remain stable for different operation loads [4,5].

This means that corrosion resistance is of secondary importance when it comes to PEMFC performance. Instead, high electrical conductivity across the interface i.e. lowest possible contact resistance becomes the most important performance parameter.

Previous studies have demonstrated low contact resistance and tuneability of thin films of nanocomposites of transition metal carbides and amorphous carbon (a-C). The amount of a-C phase strongly affects both the mechanical and electrical properties of the coatings, e.g. resulting in load-adaptive properties and low contact resistance [6–11]. Interestingly, for transition metal carbide nanocomposites a minimum in electrical resistivity and contact resistance was found for small percentages of a-C [8–10]. Using magnetron sputtering as a deposition method the amount of a-C can be readily controlled [8–12]. As titanium carbides and nitrides both have a rock salt structure and are fully miscible, film properties can be tuned further upon the addition of nitrogen [13,14]. Ti(C,N)-coatings have also demonstrated excellent corrosion resistance which was found to be a superposition of the corrosion behaviour of TiC and TiN [15,16]. Consequently, nanocomposites of titanium carbonitride and amorphous carbon are potential

<sup>\*</sup> Corresponding author.

E-mail address: [juliana.kessler@kemi.uu.se](mailto:juliana.kessler@kemi.uu.se) (J. Kessler).

candidates for coatings of bipolar plates in PEMFCs [16].

Industrially, coatings of transition metal carbonitrides are routinely deposited by physical vapour deposition (PVD). One such method is magnetron sputtering, where titanium nitride is deposited from a titanium target in a mixed argon/nitrogen atmosphere. For the deposition of titanium carbonitride coatings, carbon can be added in two possible ways: either by sputtering from a graphite target or by an additional reactive gas, namely a hydrocarbon, see e.g. Refs. [16,17]. In large scale industrial sputtering setups the use of graphite targets is typically avoided due to both a limiting low sputter yield and the brittleness of the targets. The use of a hydrocarbon gas on the other hand might introduce hydrogen to the coatings, thereby potentially changing the composition and structure of the material, especially in the a-C phase. Here, the incorporation of hydrogen leads to significant changes in the bonding of a-C.

This study aims to investigate potential differences between coatings deposited using graphite or a hydrocarbon gas as a carbon source. Here, methane was chosen as it has the highest possible hydrogen to carbon ratio enhancing potential effects from hydrogen incorporation. Additionally, the focus of the study is to identify a coating material and deposition process, which is promising for application as a multifunctional protective coating for steel BPPs in PEMFCs. Moreover, this study aims to demonstrate how mechanical and electrical properties can be tuned by depositing films with varying carbon content, and determining both structure as well as mechanical and electrical properties.

## 2. Methods

### 2.1. Synthesis

Thin films of Ti-C-N were grown by reactive pulsed DC magnetron sputtering in a Qprep500i sputter system from Mantis deposition Ltd. The system base pressure was  $< 5 \cdot 10^{-7}$  Pa. Two opposing circular 3-inch targets were arranged in a confocal sputter-down configuration. The target to substrate distance was 130 mm. To cater different characterisation methods all depositions were carried out on silicon (100), fused silica, sapphire (0001) and SS316L substrates. The substrates were cleaned in an ultrasonic bath, first in acetone then in ethanol for 5 min, and finally blown dry with nitrogen gas. Before deposition the substrates were etched in Ar atmosphere to remove surface contamination using an RF-bias of  $-120$  V for 3 min at a working pressure of 0.67 Pa. All depositions were performed at a working pressure of 0.67 Pa and at a substrate temperature of  $350^\circ\text{C}$ , determined by a calibrated thermocouple. During deposition, a RF substrate bias of  $-150$  V was applied and the substrate holder was rotating at 10 rpm. A Ti target (Testbourne Ltd, 99.995%) was used for all depositions at a constant target power of 250 W, pulsing at 200 kHz. The carbon content was varied by either changing the graphite target (Kurt J. Lesker, 99.999%) power from 20 to 170 W, or changing the gas flow of methane between 1 and 6 sccm. Methane was selected as a reactive hydrocarbon gas since it has the highest possible hydrogen to carbon ratio and would therefore enhance potential effects of incorporating hydrogen in the films. For all depositions, the total gas flow was kept constant at 60 sccm. The nitrogen gas flow was kept at 6 sccm and the flow of Ar was adjusted to compensate the methane gas flow. Deposition times were varied from 45 to 50 min to obtain  $0.4 \mu\text{m}$  thick films.

### 2.2. Characterisation

For compositional analysis, X-ray photoelectron spectroscopy (XPS) was carried out with a PHI Quantera II XPS scanning microprobe using monochromatic Al  $K\alpha$  radiation. To obtain bulk composition, depth profiles were acquired with 1 keV  $\text{Ar}^+$  ions. Then, sample composition (excluding hydrogen) was assessed by using calibrated relative sensitivity factors (RSF). Measurements were conducted on films deposited on silicon or fused silica.

For the calibration of the RSFs, and the evaluation of hydrogen content, selected samples were analysed by time-of flight energy elastic recoil detection analysis (ToF-E ERDA) using the Pelletron Accelerator at the Tandem Laboratory at Uppsala University [18]. A beam of 36 MeV  $^{127}\text{I}$  was used as primary ions with the detector placed at a scattering angle of  $45^\circ$ . For more details on the experimental system, we refer to Ref. [19]. Collected experimental spectra were analysed using the Potku software [20]. Additionally, the hydrogen concentration of two selected samples was determined by nuclear reaction analysis (NRA) to exclude any effects from beam induced hydrogen loss during ERDA. To quantify hydrogen the 6.385 MeV resonance of the  $^{15}\text{N}(^1\text{H}, \alpha\gamma)^{12}\text{C}$  nuclear reaction was used. The energy of the  $^{15}\text{N}$  primary ions was varied from 6.525 to 6.90 MeV and back to locate the resonance at different sample depths thereby acquiring a depth profile. A detailed description of the NRA analysis using the same experimental system can be found in Ref. [21]. All ion beam analysis was performed on samples deposited on fused silica substrates.

To study crystalline phases X-ray diffraction (XRD) was used, performing both  $\theta/2\theta$  and grazing incidence (GI) scans. GI-measurements were conducted on a Malvern Panalytical Empyrean diffractometer using Cu  $K\alpha$  radiation at an incident angle of  $1^\circ$  with a Göbel-mirror as primary optics and a parallel plate collimator with  $0.27^\circ$  divergence for the secondary optics. The lattice constant was determined by averaging over the 111, 200 and 220 peaks from GI-scans. Other peaks were excluded due to difficulty in separation due to line broadening. Additionally,  $\theta/2\theta$ -scans were performed for texture analysis. For XRD-analysis, films deposited on fused silica were used. For one selected sample, measurements were carried out on all available substrates to ensure that the results from silica are representative for all substrates.

Scanning electron microscopy (SEM) images were acquired of fractured cross sections from films deposited on Si substrates. A Zeiss Leo 1550 was used with the in-lens secondary electron detector at an acceleration voltage of 3 kV. The samples were tilted  $15^\circ$  to also obtain information of the surface topography.

Raman spectroscopy was performed to investigate presence and bonding of any a-C phase. A Renishaw inVia confocal Raman microscope with an excitation wavelength of 532 nm was used on films deposited on silicon. Raman spectra which showed broad D- and G-bands were fitted with two Gaussian peaks to obtain peak positions, widths of the peaks and the  $I_D/I_G$  ratio [22].

To investigate microstructure of selected samples in detail transmission electron microscopy (TEM) analysis was performed with a FEI Titan Themis 200 operated at 200 kV. Scanning transmission electron microscopy (STEM) was used for imaging. Additionally, energy dispersive X-ray spectroscopy (EDS) and electron energy loss spectroscopy (EELS) were conducted to analyse bonding and composition of the samples. Planar view TEM samples from the graphite series were prepared by mechanical polishing and low-angle  $\text{Ar}^+$  milling using a Precision ion polishing system (PIPS) from Gatan. The selected sample from the methane series was prepared using a focused ion beam (FIB) CrossBeam550 from Zeiss.

The mechanical properties were characterised with nanoindentation using a CSM Ultra Nano Hardness Tester with Berkovich diamond tip. 20 indentations were made with a maximum depth of 40 nm not to exceed 10% of the film thickness. The method proposed by Oliver & Pharr was used to calculate the hardness and elastic modulus [23]. Nanoindentation measurements were taken on films deposited on sapphire.

Resistivity was calculated from measuring the sheet resistance by four-point probe with an Advanced Instrument Technology CMT-SR2000N and then considering the thickness of the films, determined from SEM cross-sections. These measurements were carried out on samples deposited on fused silica.

The contact resistance of the films was measured against a silver-coated copper electrode using a custom-made four-point probe setup, which measures the drop in voltage while the current flows from the

**Table 1**

Composition (excluding hydrogen) as calculated from XPS depth profiles, using calibrated RSF. Indicated uncertainties are the maximum deviations of the calculated compositions from the composition obtained by ERDA.

Sample	Graphite target power/ methane gas flow	Atomic concentration (excl. H) in at.%			
		Ti ( $\pm 4$ )	N ( $\pm 3$ )	C ( $\pm 2$ )	O ( $\pm 1$ )
gra8	20 W	43	45	8	4
gra13	50 W	42	42	13	3
gra16	80 W	41	41	16	2
gra20	120 W	40	40	20	< 1
gra21	150 W	40	39	21	< 1
gra23	170 W	39	38	23	< 1
me12	1 sccm	43	41	12	4
me15	2 sccm	42	40	15	3
me18	3 sccm	41	39	18	2
me21	4 sccm	41	38	21	< 1
me34	6 sccm	35	30	34	< 1

**Table 2**

Hydrogen content of selected samples determined by ToF-E ERDA and NRA respectively.

Sample	at.% H	
	ERDA ( $\pm 0.1$ )	NRA ( $\pm 0.2$ )
gra8	0.7	n/a
gra13	0.6	n/a
gra21	< 0.05	< 0.05
me12	1.1	n/a
me21	1.4	2.5
me34	3.3	n/a

probe tip to the film surface. The samples were contacted with copper wires, and the contact force (normal load) was varied from 1 to 10 N by applying weights on a lever. The Ag-plated probe was 10 mm in diameter with a hemispherical tip. Two measurements were taken according to the van der Pauw method [24] on two points per coating. For this, coatings on stainless steel 316L substrates were used.

### 3. Results

#### 3.1. Characterisation of Ti–C–N films

Samples of titanium carbonitride with varying carbon content were deposited from two different carbon sources (graphite and methane) resulting in two samples series with increasing carbon content. These are henceforth denoted the graphite (gra) and methane (me) series, respectively. Individual samples are identified with series and a number indicating the total carbon content of the coating. Table 1 shows the average atomic bulk composition as determined through XPS depth profiling. The carbon content of the graphite series ranges from 8 to 23 at.% and for the methane series from 12 to 34 at.%. Nitrogen and titanium content decrease accordingly from 45 to 30 at.% N and from 43 to 35 at.% Ti. Additionally, it can be observed that the oxygen content decreases with an increasing carbon content from 4 to < 1 at.%.

Selected samples were analysed using ToF-E ERDA. This analysis was conducted to obtain the hydrogen content and to confirm that no other impurities were present in the coatings. Additionally, NRA was performed on two samples with a medium carbon content for hydrogen quantification: Results of the ion beam analysis are shown in Table 2. Generally, hydrogen concentrations are very low, with the graphite series showing a hydrogen content below 0.7 at.%. Sample gra21 showed no hydrogen signal above noise level. The methane series exhibits higher hydrogen concentrations, increasing with the overall carbon content from 1.05 to 3.30 at.%. Using NRA, the H concentration of sample me21 was found to be 2.5 at.%.

Fig. 1 shows GI-XRD scans of the samples from (a) graphite and (b) methane series. The dotted lines indicate the position of the 111 peak for pure TiN and TiC, with a lattice constant of 4.24 Å [25] and

4.33 Å [26], respectively. The observed reflections are indexed to a rock salt structure with a lattice constant of  $a = 4.26\text{--}4.31$  Å. As can be seen from the 111 peak, there is a shift towards smaller angles with increasing carbon content. As the peaks move from a position close to TiN towards the TiC reference, it can be concluded that the samples contain a titanium carbonitride phase. As seen in Fig. 1, peaks become less intense with increasing carbon content meaning that the samples contain a decreasing amount of crystalline phase. Moreover, the observed peak broadening with increasing carbon concentration indicates a decrease in crystallite size.

The  $\theta/2\theta$  scans (not shown) reveal a 111 texture for all deposited films, where films with a low carbon content show a higher degree of preferential orientation. Scans of films deposited on different substrates reveal a somewhat stronger 111 texture for the sapphire substrate, but otherwise no difference.

Fig. 2 shows how the lattice constant depends on the carbon content of the samples; falling between the lattice constants of TiN and TiC, as indicated by the dashed lines. It can be observed that the increase is approximately linear, which points to a substitution of N by larger C atoms thereby expanding the lattice. Moreover, the sample with the highest carbon content does not follow the same trend, indicating a possible saturation of C substitution.

Fig. 3 shows cross-sectional SEM images of selected samples. At low carbon concentrations the films consist of columns with a faceted surface; as the C content increases films become more finely grained with a smooth surface. The morphology evolution is similar for both the graphite and methane series: Increased carbon content leads to film densification, smaller crystallites and smoother top surface.

To study possible amorphous carbon phases, samples were analysed with Raman spectroscopy. Fig. 4 shows Raman spectra obtained at an excitation wavelength of 532 nm. As can be seen all samples with [C] > 13 at.% exhibit broad signals at 1370 and 1570  $\text{cm}^{-1}$ , which is consistent with the broad D- and G-bands of sputtered a-C, i.e. mainly  $\text{sp}^2$ -bonding [27,28]. Reliable peak fitting was performed for samples with a carbon content above 13 at.%. With increasing carbon content the D-peak position moved from 1370 up to 1385  $\text{cm}^{-1}$ . The G-peak position was located between 1575 and 1580  $\text{cm}^{-1}$ , independently of the carbon content. The  $I_D/I_G$ -ratio increased from 0.94 to 1.22 with increasing carbon content. No differences in intensity ratio were observed between samples with the same carbon content, deposited using different carbon sources.

In summary, the results above show that the two processes, using graphite or methane as carbon sources, produce very similar samples series with comparable composition, phases and morphology. General trends for an increasing total carbon content in both cases are the decreasing amount of crystalline titanium carbonitride phase and a decrease in crystallite size as revealed by XRD. Furthermore, SEM shows a densification of the morphology with increasing carbon concentrations for both series. Additionally, Raman analysis confirmed that the coatings contain an increasing amount of amorphous carbon, which means that the coatings are nanocomposites of Ti(C,N)/a-C.

For further characterisation, three samples were selected for TEM analysis. Fig. 5 shows the plan-view of the samples from the graphite series with 13 resp. 20 at.% carbon and a sample from the methane series with 21 at.% C. Images attained at a lower magnification using a high-angle annular dark field (HAADF) detector (Fig. 5(a)–(c)) show faceted columns for all samples as well as how the column width decreases with carbon content. Both observations are in agreement with results from SEM and XRD. In the HAADF images dark or black areas correspond to pores or a light element phase (here a-C). This confirms the densification of the film morphology observed in the SEM images. Higher magnification images acquired in bright field (BF) mode in Fig. 5(d)–(f) confirm a decrease in grain size with increasing carbon concentration. Moreover, the images clearly show the presence of two phases in both samples: heavier crystalline grains surrounded by an inter-granular lighter phase, apparently amorphous. The sample with

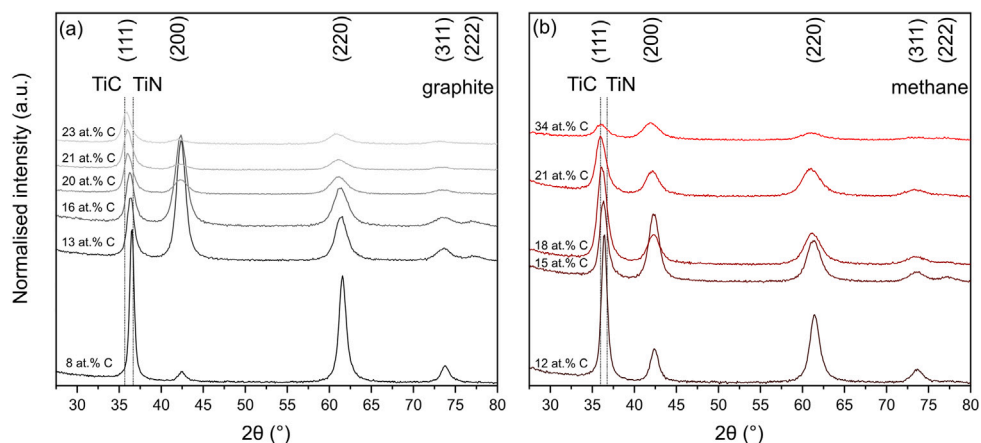


Fig. 1. GI-XRD pattern of samples deposited (a) from a graphite target and (b) under methane gas flow. Indexing for NaCl type structure, reference lines for TiN [25] and TiC [26].

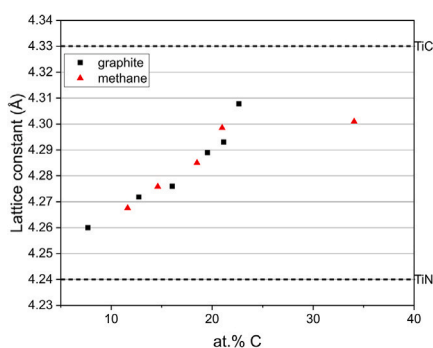


Fig. 2. The lattice constants as a function of carbon content. Dashed lines indicating the lattice constant for TiN [25] and TiC [26].

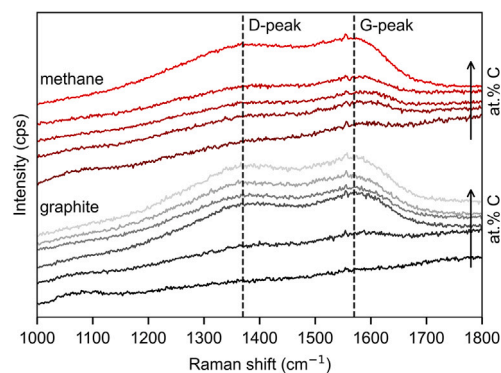


Fig. 4. Raman spectra of samples from both sample series (methane in red, graphite in grey) obtained with an excitation wavelength of 532 nm.

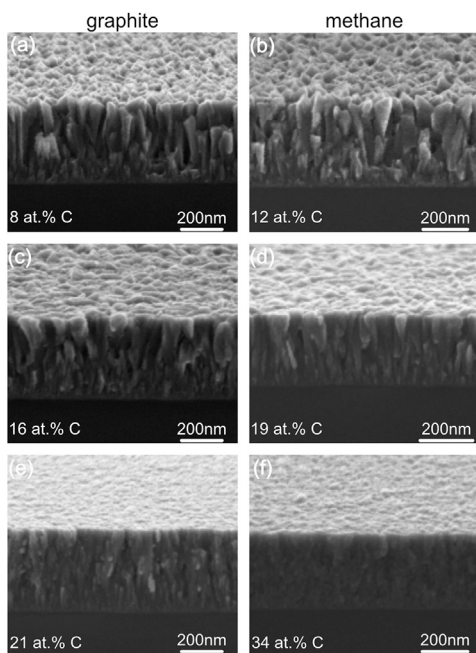


Fig. 3. Cross-sectional SEM images of samples from graphite series (a), (c), (e) and methane series (b), (d), (f) with carbon content of 8–34 at.%.

the lower carbon content contains only small amounts of the amorphous phase, which is found along some (but not all) grain boundaries.

In the samples with the higher carbon content and smaller grains, the amorphous phase decorates all grain boundaries like a tissue phase and it is found in larger amounts.

To investigate the chemical composition of the phases, EDS maps (shown in Fig. 6) were acquired. For the sample with 13 at.% C (Fig. 6(a)), the Ti and N content are closely correlated and the elements are predominantly found in the crystalline grains. Carbon can be found inside the grains in low concentrations as well as in higher concentrations along some grain boundaries. Oxygen is found only in the grain boundaries. Line scans over grain boundaries (not shown) reveal that the N concentration drops as the oxygen concentration increases which points to that oxidation takes place mostly in the grain boundaries. For the higher carbon content samples (see Fig. 6(b) and (c)), the Ti content again correlates to the grain structure. The grain structure appears less distinct for the sample deposited with methane. This is an artefact due to an increased TEM-lamella thickness of this particular sample resulting in higher count rates of titanium compared to the lighter elements. The nitrogen signal for both high C-content samples, however, is flat and contrary to the sample with lower C content it does not correlate to the Ti concentration. Again, carbon is found in low concentrations in the grains and predominantly located in the grain boundaries. Consequently, the amorphous tissue phase must also contain some nitrogen. Oxygen is also located in the grain boundaries but in lower concentration as compared to sample with lower carbon concentration, note the different concentration colour scale in Fig. 6.

A comparison of EELS nitrogen edge spectra from within the grain and in the grain boundaries (not shown) confirms the difference in nitrogen signal shown by the EDS maps. The amorphous phase does

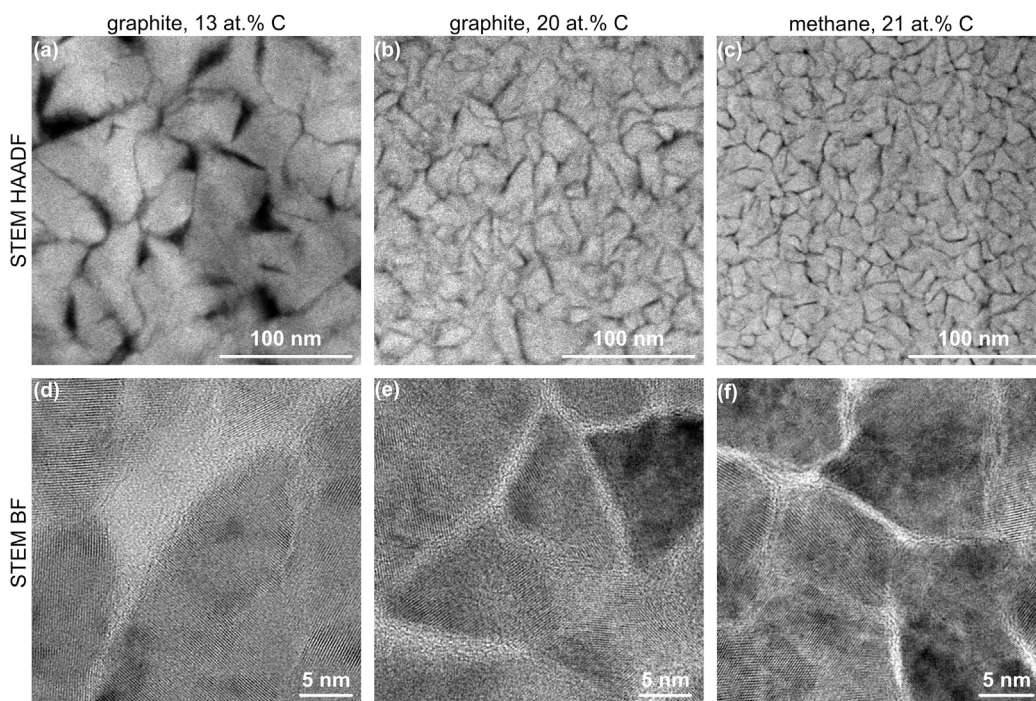


Fig. 5. STEM images of samples gra13 (a, d), gra20 (b, e) and me21 (c, f) acquired in HAADF mode and in BF mode.

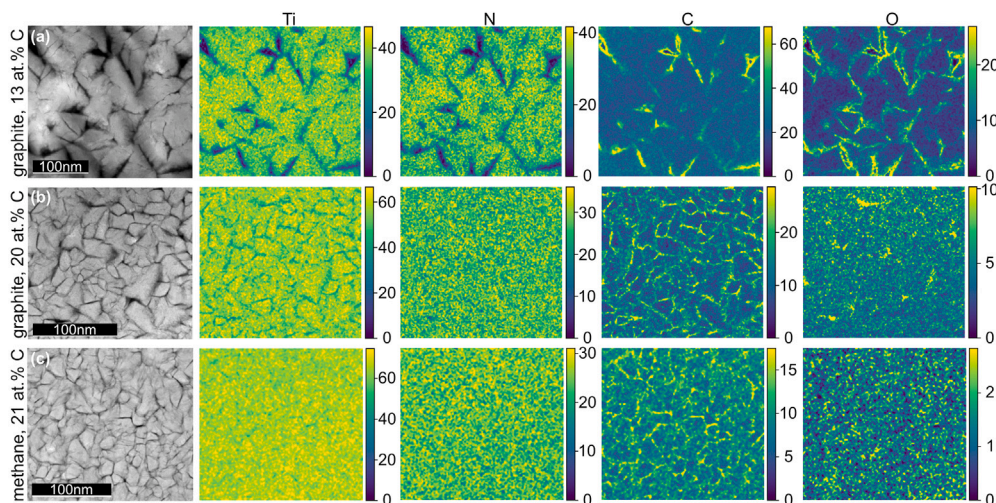


Fig. 6. HAADF images and EDS maps of samples (a) gra13, (b) gra20 and (c) me21. Note the different concentration colour scales for each samples. The reduced visibility of grain boundaries in the Ti-map of sample me21 (c) is due to larger TEM-lamella thickness resulting in an increased Ti-signal compared to the lighter elements.

not contain nitrogen for the sample with lower carbon concentration. Contrarily, for the samples with higher C content a weak N signal can always be observed in the amorphous phase.

TEM analysis of selected samples corroborates that the samples consist of nanocrystalline titanium carbonitride nc-Ti(C,N) and an amorphous carbon phase, generally denoted as a-C(:N). The a-C(:N) phase was found to be a tissue phase along the grain boundaries, fully decorating for larger C content and partially decorating for lower C concentration. Furthermore, the analysis indicates that the amorphous carbon phase contains some nitrogen for samples with higher C content, but not for the sample with lower carbon concentration. The comparison between samples with [C] > 20 at.% from both series confirms that the microstructure is mainly dependent on the carbon content and that the choice of carbon source has no or a very small influence.

### 3.2. Properties

Mechanical properties of the films were evaluated by nanoindentation. The results are presented in Fig. 7 as a function of carbon content. The hardness varies between 11 and 38 GPa with peak hardness at around 20 at.% carbon for both series. Young's modulus varies from 312 to 536 GPa, with a maximum at around 20 at.% C for both sample series.

Using a four-point probe, the electrical resistivity of the samples was determined. The results are presented in Fig. 8 as a function of carbon concentration. The resistivity of most samples is in the same order of magnitude, 150–280  $\mu\Omega$  cm. Only the sample with the highest carbon content shows a significant resistivity of 623  $\mu\Omega$  cm.

Contact resistance measured at a contact force of 5 N is shown in Fig. 9 as a function of carbon concentration. For the graphite series, the contact resistance ranges from 7 to 15 m $\Omega$  and the methane series

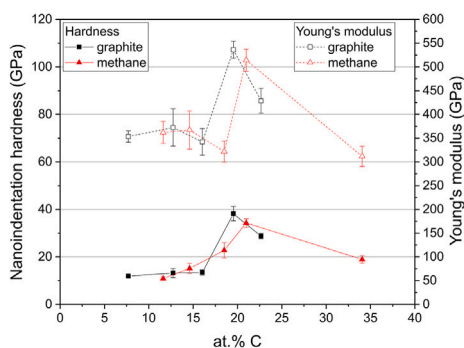


Fig. 7. Nanoindentation hardness and Young's modulus as a function of carbon content. Lines are only intended as guides for the eyes.

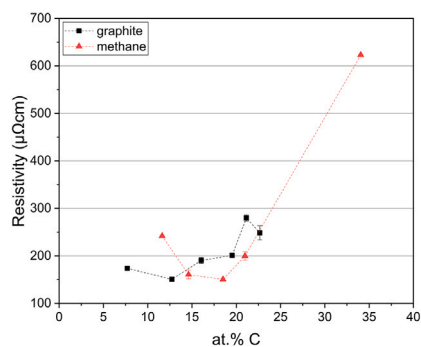


Fig. 8. Resistivity as a function of carbon content. Lines are only intended as guides for the eyes.

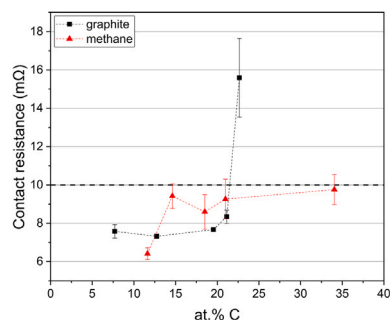


Fig. 9. Contact resistance measured at a contact force of 5 N as a function of carbon concentration. The dashed line indicates the DOE target of 10 mΩ for bipolar plates in PEMFC.

varies from 6 to 10 mΩ. It can be observed that the contact resistance increases with carbon concentration. The dashed line at 10 mΩ indicates a target value set by the US-department of Energy (DOE) for the interfacial contact resistance on bipolar plates for fuel cells at a load of 140 N/mm<sup>2</sup> [29]. Although not measured accordingly, an indication of performance in contact resistance is given by comparison with the DOE-target. Compared to the stainless steel reference (not shown) with a measured contact resistance of 98 mΩ at 5 N, all samples show a significantly improved contact resistance.

#### 4. Discussion

Two series of Ti-C-N coatings with varying carbon content were produced by magnetron sputtering using graphite and methane as carbon sources, respectively. Generally, the two series are found to be comparable in terms of composition, phases and microstructure.

#### 4.1. Microstructural evolution and composition

Considering results from XRD, Raman and TEM analysis it is clear that the coatings are nanocomposites of nanocrystalline titanium carbonitride and an amorphous carbon phase, i.e. nc-Ti(C,N)/a-C(:N). The microstructure and morphology is found to depend mainly on the carbon content not the choice of carbon source. A similar morphology evolution with a decrease in crystallite size and smoothening of the surface is observed with increasing C concentration for both series. This morphology evolution and decreased crystallite size is well in line with observations in related carbide systems [11] as well as a more general model presented by Barna and Adamik [30] for the addition of elements forming an amorphous tissue or matrix phase. Although only observed in the selected TEM samples, it is safe to assume that a-C(:N) is present in all coatings with [C] ≥ 20 at.%. At lower carbon concentrations, a-C(:N) decorates some of the grain boundaries. As carbon content and the amount of a-C(:N) phase increase the coverage increases forming first a tissue phase and eventually a matrix phase in which the carbonitride grains are embedded. However, a threshold value for the formation of a tissue phase could not be clearly identified.

Ion beam analysis shows a very low concentration of H for the samples deposited from a graphite target, which is believed to stem only from residual hydrogen in the deposition chamber. As expected, the samples using methane as carbon source exhibit somewhat higher hydrogen concentrations, increasing with the overall carbon content. However, hydrogen concentrations are generally very low (below 4 at.% H) also for samples deposited using methane as a carbon source. A contributing factor for this is probably the elevated substrate temperature of 350°C, which promotes hydrogen desorption during the deposition. NRA of a selected sample shows a slightly higher H-content (2.5 at.%) compared to the concentration determined by ToF-E ERDA (1.4 at.%). This indicates ion beam induced hydrogen loss during ERDA. The depth profile acquired during NRA confirms that there is no beam induced hydrogen loss during this measurement.

For the samples with a carbon content up to 18 at.% C there is an appreciable oxygen content (up to 4 at.%) observed in the XPS depth profiles. This is deemed to be the result of ex-situ oxidation occurring when the samples are exposed to atmosphere after deposition and caused by the underdense microstructure observed in electron microscopy for these samples. This is supported by the high resolution EDS maps presented in 6. Here it is observed that oxidation occurs in many grain boundaries of the underdense sample with low carbon content, but not in the bulk of the carbonitride phase. For the denser samples with higher carbon content the oxygen signal is generally much lower, and only a few spots along grain boundaries show signs of oxidation. The a-C(:N) tissue phase clearly protects the nc-Ti(C,N) grains from oxidation.

For a more detailed understanding of the material and structure-property correlations, one would like to determine a number of key parameters, including composition of respective phase and their relative amounts. However, as will be discussed below, this is in the present case difficult.

#### 4.2. Titanium carbonitride phase

From XRD and TEM it is clear that the majority phase of the coatings is a nanocrystalline titanium carbonitride, nc-Ti(C,N), where the crystallite size decreases with increased carbon content. Both the expansion of lattice parameter observed from XRD and elemental maps by high resolution EDS show that carbon is incorporated into the nitride phase as total carbon content is increased. It is however difficult to determine the composition of the nc-Ti(C,N) phase. A common method is to use Vegard's law [31] to determine the stoichiometry, based on the observed lattice parameter. The here observed lattice parameter is, however, larger than expected considering the total composition of the samples. Possible reasons include residual stresses or influence of the

surrounding a-C(:N) tissue phase on the bonding of nc-Ti(C,N). Such an influence has been shown by Lewin et al. for the related nc-TiC<sub>x</sub>/a-C system [32]. A similar effect could also be present in the carbonitride system, although one must consider their different electronic structures. To determine the Ti(C,N) composition directly from the TEM EDS maps is not reliable due to the nanocrystalline nature of the phase which causes overlap issues with the tissue phase. Along with that, difficulties in determining the composition and amount of the a-C(:N) phase (see below) make a calculation based on the total composition unfeasible.

#### 4.3. Amorphous tissue phase

Raman spectroscopy and TEM-EDS show that coatings contain an a-C(:N) phase and that the amount increases with total carbon content. Additionally, EELS analysis reveals that N present in the a-C(:N) phase has different bonding characteristics than the nitrogen in the crystalline phase. Analysis of the Raman spectra shows that the observed peak positions and intensity ratios are well in line with literature on sputtered a-C [27,28,33–35]. The differences in peak position and  $I_D/I_G$  between the series are negligible, despite the use of different carbon sources. Compared to the three-stage model of G-peak position and  $I_D/I_G$  ratio as a function of the amorphisation of graphite presented by Ferrari and Robertson [22], the present coatings are similar to stage two: partial amorphisation of carbon. Thus, it can be concluded that the a-C(:N) phase is dominated by  $sp^2$ -bonding, which agrees well with the observed low hydrogen content. Generally, Casiraghi, Ferrari and Robertson [34] found that concentrations below 20 at.% are too low to cause measurable structural and topological disordering. The films can hence be treated as H-free. Compared to literature on sputtered a-C, the D- and G-peaks are found to be broader. This broadening is in agreement with observations of nitrogen doped a-C films [36,37] and can thus be attributed to the presence of nitrogen in the a-C(:N) tissue phase.

#### 4.4. Relative amount of phases

A quantification of the relative amount of a-C phase would be an excellent parameter to relate structure and properties. Raman spectroscopy is useful to identify a-C phases, but does not provide an easy quantification of a-C relative to other phases. XPS is routinely used to quantify the relative amounts of a-C and carbide phase for transition metal carbide/a-C nanocomposites [8,10,11,38]. However, initial analysis (not presented) of the Ti–C–N samples has shown considerable artefacts from Ar<sup>+</sup> etching in the C 1s spectra. These are more severe than those observed in the Ti–C system [39,40] and this correlates well with general sensitivity of transition metal nitrides [41]. Thus, the matter of a-C quantification in the Ti–C–N system is not included here, and it will be the subject of further studies.

#### 4.5. Coating properties

The obtained hardness values show a maximum of 38 and 34 GPa for graphite and methane respectively at around 20 at.% carbon. The peak hardness coincides with a maximum in Young's modulus at the same carbon concentration. The mechanical properties of the films are well in line with literature for related TiN, TiC, TiC/a-C and Ti(C,N) films [11,12,35,42]. The comparably lower hardness values for films with low carbon content are attributed to the somewhat underdense microstructure of these films. Similar peak hardness as a function of carbon content has been observed for nanocomposites of TiC and a-C(:H) [9,38,43]. The same is observed for the given Ti(C,N)/a-C(:N): First, the formation of a-C(:N) leads to nano-hardening, as dislocations are trapped in grain boundaries. Secondly, a-C(:N) is considerably softer than Ti(C,N). An increased amount of a-C(:N) will accordingly lead to a softer coating. The somewhat stronger 111 texture observed for coatings on sapphire may affect the hardness. Thus, it is possible

that the coatings on other substrates such as steel have a slightly different hardness. Considering the microstructure observed by SEM and TEM (Figs. 3 and 5), this most likely only affects samples with a low carbon concentration.

The measured resistivity values are in same order of magnitude as reports of polycrystalline TiN and TiC(/a-C) films in literature [9,43,44]. The observed trends in resistivity can also be explained by the formation of a-C(:N). Once the more resistive tissue phase is formed and encapsulates the conducting Ti(C,N) grains, resistivity is expected to increase with an increasing amount of a-C(:N). As shown in Fig. 8, the trends are not linear. For the series deposited with methane for example, there is a minimum resistivity detected at around 20 at.% carbon. This is attributed to the slightly underdense columnar microstructure of the coatings. Here, the a-C(:N) fills the voids between grains, reducing post deposition oxidation and thereby effectively improving conductivity in the direction of measurement.

The contact resistance of the coatings was found to be significantly improved by one order of magnitude compared to a stainless steel reference. Only small variations were found as a function of carbon content within the studied range of 8–34 at.% C. Again, the choice of carbon source does not result in a significant difference between the contact resistance of the two sample series. Contact resistance is dependent on both the mechanical and electrical properties of the coatings: A softer coating would lead to an increased contact area thereby reducing contact resistance. The resistivity of the coatings represents the bottom limit of the contact resistance in an ideal electrical contact. Additionally, the tissue phase will effectively increase the contact area on the surface of the coatings resulting in a reduced contact resistance. Therefore, the contact resistance of Ti(C,N)/a-C(:N) would be expected to be at its minimum for around 15 to 20 at.% carbon, where the resistivity is at its minimum, hardness has not yet reached its peak and a tissue phase of a-C(:N) has formed.

Considering these results as well as literature reports on corrosion resistance of Ti–C–N films [15,16], coatings of Ti(C,N)/a-C(:N) are promising candidates for the coating of bipolar plates for PEMFCs. This is particularly true as this material system shows considerable tuneability where mechanical and electrical properties can be designed by control of the carbon content.

A valuable finding considering possible industrial applications where deposition rate is an important parameter, is that coatings deposited from graphite and methane show similar compositions, microstructure and morphology evolution, as well as mechanical and electrical properties at similar carbon concentrations. This means that the choice of carbon source is not crucial for the film properties. It can therefore be concluded that the industrially more attractive process using a hydrocarbon gas as source of carbon can achieve equivalent results as compared to the use of a graphite target. Industrially, other interesting options include the use of acetylene gas or composite targets, the investigation of which is beyond the scope of the present study.

## 5. Concluding remarks

The two studied deposition processes produced very similar sample series, with comparable performance. The deposited Ti–C–N coatings with carbon contents between 8 and 34 at.% were found to be nanocomposites of a nanocrystalline NaCl-type titanium carbonitride and an amorphous carbon phase with mainly  $sp^2$ -bonding. Hydrogen incorporation is generally small, < 1 at.% for the samples deposited with a graphite target, and < 4 at.% for the samples deposited from methane gas, and no direct influence on material properties was observed. The determining factor for the properties was instead found to be the total carbon content, which controls both the relative amount of the two phases and the crystallite size of the carbonitride. Depending on carbon content the hardness was found to vary between 11 and 38 GPa, with a peak hardness around 20 at.% C which coincides with

a full coverage of tissue phase and thus agrees well with previously observed nanocomposite hardening. The resistivity of the coatings increases due to underdense coatings at low carbon content and due to the low conductivity of the a-C phase at high carbon content. The combination of mechanical and electrical properties leads to electrical contact resistances that at best are 10 times lower than that of a stainless steel reference. An optimum is expected around 15 to 20 at.% carbon. Here, the resistivity is at its minimum, and hardness has not yet reached its peak, but some of a-C tissue phase has formed making for a larger contact area. Considering the observed electrical contact performance, the tuneability of the nanocomposite morphology, as well as the well-known corrosion resistance of titanium carbonitride, sputter deposited Ti–C–N coatings are promising candidates for use as multifunctional protective coatings on bipolar plates in fuel cells and similar applications.

### CRedit authorship contribution statement

**Juliana Kessler:** Writing – original draft, Investigation, Formal analysis. **Olivier Donzel-Gargand:** Writing – review & editing, Investigation, Formal analysis. **Dmitrii Moldarev:** Writing – review & editing, Investigation, Formal analysis. **Claudia Franzén:** Investigation. **Daniel Primetzhofer:** Supervision, Investigation. **Ulf Jansson:** Writing – review & editing, Funding acquisition, Conceptualization. **Erik Lewin:** Writing – review & editing, Supervision, Conceptualization.

### Declaration of competing interest

The authors declare that they have no known competing financial interests or personal relationships that could have appeared to influence the work reported in this paper.

### Acknowledgements

The work was supported financially by the VINNOVA Competence Centre FunMat-II (Grant No. 2022-03071) and we acknowledge Myfab Uppsala for providing facilities and experimental support. Myfab is funded by the Swedish Research Council (Grant No. 2020-00207) as a national research infrastructure. Furthermore, infrastructure support by VR-RFI (Grant No. 2019-00191) supporting accelerator operation is gratefully acknowledged. We also acknowledge Alleima AB for providing stainless steel substrates as well as Jörgen Westlinder for insightful discussions of the results.

### Data availability

Data will be made available on request.

### References

- [1] X. Li, I. Sabir, Review of bipolar plates in PEM fuel cells: Flow-field designs, *Int. J. Hydrog. Energy* 30 (4) (2005) 359–371, <http://dx.doi.org/10.1016/j.ijhydene.2004.09.019>.
- [2] H. Tawfik, Y. Hung, D. Mahajan, Metal bipolar plates for PEM fuel cell—A review, *J. Power Sources* 163 (2) (2007) 755–767, <http://dx.doi.org/10.1016/j.jpowsour.2006.09.088>.
- [3] S. Karimi, N. Fraser, B. Roberts, F.R. Foulkes, A review of metallic bipolar plates for proton exchange membrane fuel cells: Materials and fabrication methods, *Adv. Mater. Sci. Eng.* 2012 (1) (2012) 828070, <http://dx.doi.org/10.1155/2012/828070>.
- [4] L. Castanheira, M. Bedouet, A. Kucernak, G. Hinds, Influence of microporous layer on corrosion of metallic bipolar plates in fuel cells, *J. Power Sources* 418 (2019) 147–151, <http://dx.doi.org/10.1016/j.jpowsour.2019.02.005>.
- [5] T. Novalin, B. Eriksson, S. Proch, U. Bexell, C. Moffatt, J. Westlinder, C. Lagergren, G. Lindbergh, R. Wreland Lindström, Concepts for preventing metal dissolution from stainless-steel bipolar plates in PEM fuel cells, *Energy Convers. Manage.* 253 (2022) 115153, <http://dx.doi.org/10.1016/j.enconman.2021.115153>.
- [6] A.A. Voevodin, J.S. Zabinski, Load-adaptive crystalline–amorphous nanocomposites, *J. Mater. Sci.* 33 (2) (1998) 319–327, <http://dx.doi.org/10.1023/A:1004307426887>.
- [7] D. Martínez-Martínez, J.C. Sánchez-López, Determination of the thickness of the embedding phase in OD nanocomposites, *Appl. Surf. Sci.* 421 (2017) 179–184, <http://dx.doi.org/10.1016/j.apsusc.2016.12.081>.
- [8] E. Lewin, O. Wilhelmsson, U. Jansson, Nanocomposite nc-TiC/a-C thin films for electrical contact applications, *J. Appl. Phys.* 100 (5) (2006) 054303, <http://dx.doi.org/10.1063/1.2336302>.
- [9] E. Lewin, E. Olsson, B. André, T. Joelsson, Å. Öberg, U. Wiklund, H. Ljungcrantz, U. Jansson, Industrialisation study of nanocomposite nc-TiC/a-C coatings for electrical contact applications, *Plasma Process. Polym.* 6 (S1) (2009) <http://dx.doi.org/10.1002/ppap.200932303>.
- [10] N. Nedfors, O. Tengstrand, E. Lewin, A. Furlan, P. Eklund, L. Hultman, U. Jansson, Structural, mechanical and electrical-contact properties of nanocrystalline-NbC/amorphous-C coatings deposited by magnetron sputtering, *Surf. Coat. Technol.* 206 (2–3) (2011) 354–359, <http://dx.doi.org/10.1016/j.surfcoat.2011.07.021>.
- [11] U. Jansson, E. Lewin, Sputter deposition of transition-metal carbide films — A critical review from a chemical perspective, *Thin Solid Films* 536 (2013) 1–24, <http://dx.doi.org/10.1016/j.tsf.2013.02.019>.
- [12] H. Larhlimi, A. Ghailane, M. Makha, J. Alami, Magnetron sputtered titanium carbide-based coatings: A review of science and technology, *Vacuum* 197 (2022) 110853, <http://dx.doi.org/10.1016/j.vacuum.2021.110853>.
- [13] H. Holleck, Material selection for hard coatings, *J. Vac. Sci. Technol. A: Vac. Surf. Films* 4 (6) (1986) 2661–2669, <http://dx.doi.org/10.1116/1.573700>.
- [14] S.-H. Jhi, J. Ihm, S.G. Louie, M.L. Cohen, Electronic mechanism of hardness enhancement in transition-metal carbonitrides, *Nature* 399 (6732) (1999) 132–134, <http://dx.doi.org/10.1038/20148>.
- [15] L. von Fieandt, K. Johansson, E. Lindahl, T. Larsson, M. Boman, D. Rehnlund, Corrosion properties of CVD grown Ti(C,N) coatings in 3.5 wt-% NaCl environment, *Corros. Eng. Sci. Technol.* 53 (4) (2018) 316–320, <http://dx.doi.org/10.1080/1478422X.2018.1467150>.
- [16] J. Jin, J. Zhang, M. Hu, X. Li, Investigation of high potential corrosion protection with titanium carbonitride coating on 316L stainless steel bipolar plates, *Corros. Sci.* 191 (2021) 109757, <http://dx.doi.org/10.1016/j.corsci.2021.109757>.
- [17] V. Anusha Thampi, B. Subramanian, Enhancement of bioactivity of pulsed magnetron sputtered TiCxNy with bioactive glass (BAG) incorporated polycaprolactone (PCL) composite scaffold, *J. Alloys Compd.* 649 (2015) 1210–1219, <http://dx.doi.org/10.1016/j.jallcom.2015.06.250>.
- [18] P. Ström, D. Primetzhofer, Ion beam tools for nondestructive in-situ and in-operando composition analysis and modification of materials at the Tandem Laboratory in Uppsala, *J. Instrum.* 17 (04) (2022) P04011, <http://dx.doi.org/10.1088/1748-0221/17/04/P04011>.
- [19] P. Ström, P. Petersson, M. Rubel, G. Possnert, A combined segmented anode gas ionization chamber and time-of-flight detector for heavy ion elastic recoil detection analysis, *Rev. Sci. Instrum.* 87 (10) (2016) 103303, <http://dx.doi.org/10.1063/1.4963709>.
- [20] K. Arstila, J. Julin, M.I. Laitinen, J. Aalto, T. Konu, S. Kärkkäinen, S. Rahkonen, M. Raunio, J. Itkonen, J.P. Santanen, T. Tuovinen, T. Sajavaara, Potku – New analysis software for heavy ion elastic recoil detection analysis, *Nucl. Instrum. Methods Phys. Res. B* 331 (2014) 34–41, <http://dx.doi.org/10.1016/j.nimb.2014.02.016>.
- [21] K. Komander, M.V. Moro, S.A. Droulias, J. Muggenburg, G.K. Pálsson, T. Nyberg, D. Primetzhofer, M. Wolff, Hydrogen site location in ultrathin vanadium layers by N-15 nuclear reaction analysis, *Nucl. Instrum. Methods Phys. Res. B* 455 (2019) 57–60, <http://dx.doi.org/10.1016/j.nimb.2019.05.033>.
- [22] A.C. Ferrari, J. Robertson, Interpretation of Raman spectra of disordered and amorphous carbon, *Phys. Rev. B* 61 (20) (2000) 14095–14107, <http://dx.doi.org/10.1103/PhysRevB.61.14095>.
- [23] W.C. Oliver, G.M. Pharr, An improved technique for determining hardness and elastic modulus using load and displacement sensing indentation experiments, *J. Mater. Res.* 7 (6) (1992) 1564–1583, <http://dx.doi.org/10.1557/JMR.1992.1564>.
- [24] L.J. van der Pauw, A method of measuring specific resistivity and hall effect of discs of arbitrary shape, *Philips Res. Rep.* 13 (1) (1958) 1–9.
- [25] W. Wong-Ng, H.F. McMurdie, B. Paretzkin, C.R. Hubbard, A.L. Dragoo, J.M. Stewart, Standard X-ray diffraction powder patterns of fifteen ceramic phases, *Powder Diffr.* 2 (2) (1987) 106–117, <http://dx.doi.org/10.1017/S0885715600012495>.
- [26] M.C. Morris, H.F. McMurdie, E.H. Evans, B. Paretzkin, H.S. Parker, N.C. Panagiotopoulos, C.R. Hubbard, *Standard X-ray diffraction powder patterns: Section 18. Data for 58 substances*, 1981.
- [27] J. Schwan, S. Ulrich, V. Batori, H. Ehrhardt, S.R.P. Silva, Raman spectroscopy on amorphous carbon films, *J. Appl. Phys.* 80 (1) (1996) 440–447, <http://dx.doi.org/10.1063/1.362745>.
- [28] A.C. Ferrari, J. Robertson, Raman spectroscopy of amorphous, nanostructured, diamond-like carbon, and nanodiamond, in: A.C. Ferrari, J. Robertson (Eds.), *Philos. Trans. R. Soc. Lond. Ser. A Math. Phys. Eng. Sci.* 362 (1824) (2004) 2477–2512, <http://dx.doi.org/10.1098/rsta.2004.1452>.

- [29] Energy.gov, DOE technical targets for polymer electrolyte membrane fuel cell components, 2024, URL <https://www.energy.gov/eere/fuelcells/doe-technical-targets-polymer-electrolyte-membrane-fuel-cell-components>. (accessed 21 November 2024).
- [30] P.B. Barna, M. Adamik, Fundamental structure forming phenomena of polycrystalline films and the structure zone models, *Thin Solid Films* 317 (1) (1998) 27–33, [http://dx.doi.org/10.1016/S0040-6090\(97\)00503-8](http://dx.doi.org/10.1016/S0040-6090(97)00503-8).
- [31] L. Vegard, Die konstitution der mischkristalle und die raumfüllung der atome, *Z. Phys.* 5 (1) (1921) 17–26, <http://dx.doi.org/10.1007/BF01349680>.
- [32] E. Lewin, M. Räsander, M. Klintonberg, A. Bergman, O. Eriksson, U. Jansson, Design of the lattice parameter of embedded nanoparticles, *Chem. Phys. Lett.* 496 (1–3) (2010) 95–99, <http://dx.doi.org/10.1016/j.cplett.2010.07.013>.
- [33] M.A. Tamor, W.C. Vassell, Raman “fingerprinting” of amorphous carbon films, *J. Appl. Phys.* 76 (6) (1994) 3823–3830, <http://dx.doi.org/10.1063/1.357385>.
- [34] C. Casiraghi, A.C. Ferrari, J. Robertson, Raman spectroscopy of hydrogenated amorphous carbons, *Phys. Rev. B* 72 (8) (2005) 085401, <http://dx.doi.org/10.1103/PhysRevB.72.085401>.
- [35] D. Martínez-Martínez, C. López-Cartes, A. Fernández, J.C. Sánchez-López, Influence of the microstructure on the mechanical and tribological behavior of TiC/a-C nanocomposite coatings, *Thin Solid Films* 517 (5) (2009) 1662–1671, <http://dx.doi.org/10.1016/j.tsf.2008.09.091>.
- [36] N. Hellgren, M.P. Johansson, E. Broitman, L. Hultman, J.-E. Sundgren, Role of nitrogen in the formation of hard and elastic CN<sub>x</sub> thin films by reactive magnetron sputtering, *Phys. Rev. B* 59 (7) (1999) 5162–5169, <http://dx.doi.org/10.1103/PhysRevB.59.5162>.
- [37] B. Kleinsorge, A.C. Ferrari, J. Robertson, W.I. Milne, S. Waidmann, S. Hearne, Bonding regimes of nitrogen in amorphous carbon, *Diam. Relat. Mater.* 9 (3) (2000) 643–648, [http://dx.doi.org/10.1016/S0925-9635\(99\)00309-X](http://dx.doi.org/10.1016/S0925-9635(99)00309-X).
- [38] T. Zehnder, J. Patscheider, Nanocomposite TiC/a-C:H hard coatings deposited by reactive PVD, *Surf. Coat. Technol.* 133–134 (2000) 138–144, [http://dx.doi.org/10.1016/S0257-8972\(00\)00888-4](http://dx.doi.org/10.1016/S0257-8972(00)00888-4).
- [39] E. Lewin, P. Persson, M. Lattemann, M. Stüber, M. Gorgoi, A. Sandell, C. Ziebert, F. Schäfers, W. Braun, J. Halbritter, S. Ulrich, W. Eberhardt, L. Hultman, H. Siegbahn, S. Svensson, U. Jansson, On the origin of a third spectral component of C1s XPS-spectra for nc-TiC/a-C nanocomposite thin films, *Surf. Coat. Technol.* 202 (15) (2008) 3563–3570, <http://dx.doi.org/10.1016/j.surfcoat.2007.12.038>.
- [40] E. Lewin, M. Gorgoi, F. Schäfers, S. Svensson, U. Jansson, Influence of sputter damage on the XPS analysis of metastable nanocomposite coatings, *Surf. Coat. Technol.* 204 (4) (2009) 455–462, <http://dx.doi.org/10.1016/j.surfcoat.2009.08.006>.
- [41] G. Greczynski, D. Primetzhofer, J. Lu, L. Hultman, Core-level spectra and binding energies of transition metal nitrides by non-destructive x-ray photoelectron spectroscopy through capping layers, *Appl. Surf. Sci.* 396 (2017) 347–358, <http://dx.doi.org/10.1016/j.apsusc.2016.10.152>.
- [42] L. Karlsson, L. Hultman, M.P. Johansson, J.E. Sundgren, H. Ljungcrantz, Growth, microstructure, and mechanical properties of arc evaporated TiC<sub>x</sub>N<sub>1-x</sub> (0 ≤ x ≤ 1) films, *Surf. Coat. Technol.* 126 (1) (2000) 1–14, [http://dx.doi.org/10.1016/S0257-8972\(00\)00518-1](http://dx.doi.org/10.1016/S0257-8972(00)00518-1).
- [43] W. Gulbiński, S. Mathur, H. Shen, T. Suszko, A. Gilewicz, B. Warcholiński, Evaluation of phase, composition, microstructure and properties in TiC/a-C:H thin films deposited by magnetron sputtering, *Appl. Surf. Sci.* 239 (3) (2005) 302–310, <http://dx.doi.org/10.1016/j.apsusc.2004.05.278>.
- [44] L. Toth, *Transition Metal Carbides and Nitrides*, Elsevier Science & Technology, San Diego, UNITED STATES, 1971.